RSC Advances

PAPER

View Article Online
View Journal | View Issue

Check for updates

Cite this: *RSC Adv.*, 2017, **7**, 26650

Metal chloride-assisted synthesis of hierarchical porous carbons for high-rate-performance supercapacitor

Xuefeng Bing,[a] Xu Jiang,[a] Meng Tian,[a] Jitong Wang,*[ac] Wenming Qiao[ab] and Licheng Ling*[ab]

Hierarchical porous carbons with high surface area were prepared by direct carbonization of the polymers which were synthesized *via* a typical sol–gel method, using terephthalaldehyde and resorcinol as carbon precursors, and metal chloride as reaction assistant. All the metal chlorides could efficiently help to form 3-D porous network carbon with inter-linking irregular particles, and also successfully contribute to the developing of meso-macropores through the packing of grains. Such hierarchical porosity plays an important role for rapid ion diffusion, resulting in an excellent rate capability and low diffusion resistance. Moreover, it should be noted that $ZnCl_2$ could also act as an *in situ* activation agent during the carbonization process to generate large surface area of 1106 $m^2\ g^{-1}$ and pore volume of 1.2 $cm^3\ g^{-1}$. In 3 mol L^{-1} H_2SO_4, high specific capacitance of 174.6 F g^{-1} by using the $ZnCl_2$-assisted hierarchical porous carbon as electrode material is obtained and it could retain *ca.* 84% when the current density increases from 0.1 A g^{-1} to 20 A g^{-1}. This superior rate capability is higher than that of many hierarchical porous carbons reported in previous literatures. The facile production and excellent electrochemical performance suggested a low cost and effective method to prepare hierarchical porous carbon for energy storage.

Received 10th April 2017
Accepted 10th May 2017

DOI: 10.1039/c7ra04075j

rsc.li/rsc-advances

Open Access Article. Published on 18 May 2017. Downloaded on 11/25/2024 9:47:15 PM.
This article is licensed under a Creative Commons Attribution-NonCommercial 3.0 Unported Licence.

1 Introduction

Porous carbon materials have attracted widespread attention in modern technological applications, such as gas adsorption,[1,2] catalyst supports,[3,4] medicaments[5,6] and energy storage,[7,8] owing to their high surface area, excellent stability and high conductivity. Generally, the properties of porous carbons are determined by the pore size distribution, surface area, surface chemistry and architecture.[9,10] As the electrode materials for supercapacitor, porous carbons should possess high specific surface area which could adsorb plenty of ions to achieve high specific capacitance, and developed porosity which could accelerate ion diffusion to improve power density and rate capability.[11–15]

Previous researches suggested that hierarchical porous carbons with micro-meso-macroporous structures are among the most favorable porous carbons for electrochemical applications due to the synergetic effects of multi-scale pores. In such structure, the micropores could provide high surface area for large amounts of ions to be adsorbed, mesopores could accelerate ion diffusion, while the macropores could store electrolyte to shorten the distance of ion diffusion.[16–20] Up to date, hierarchical porous carbons can be prepared by various methods, such as multi-template synthesis, bio-inspired methods and chlorination of titanium-carbide–carbon composites.[21–26] Among them, the most applicable synthetic procedure is the templating approaches by sacrificial templates, such as P123, aluminosilicate, colloidal silica and zeolite.[25–29] Hierarchical porous carbons with pore size ranging from 3 nm to 100 nm were synthesized using hierarchical silica capsules as the hard template and triblock copolymer Pluronic P123 as the soft template.[18] Such porous carbon with specific surface area of 760 $m^2\ g^{-1}$ had a high specific capacitance of 170 F g^{-1} and excellent cycling stability for 5000 cycles. Liu *et al.*[19] prepared the hierarchical hollow porous carbon using multi-templates. The porous carbon with surface area of 669 $m^2\ g^{-1}$ showed a high specific capacitance of 240 F g^{-1}, and further activation process could improve the surface area to 1290 $m^2\ g^{-1}$ and increase the specific capacitance to 304 F g^{-1}. All the results suggested that the developed hierarchical porosity could enhance the electrochemical performance and the increase of micropores effectively contributed to the improvement of capacitance. Nevertheless, additional steps to remove templates

[a]State Key Laboratory of Chemical Engineering, East China University of Science and Technology, Shanghai, 200237, P. R. China. E-mail: lchling@ecust.edu.cn; Fax: +86 21 64252914; Tel: +86 21 64252924

[b]Key Laboratory of Specially Functional Polymeric Materials and Related Technology, East China University of Science and Technology, Shanghai, 200237, P. R. China

[c]National Engineering Research Center of Ultrafine Powder, East China University of Science and Technology, Shanghai, 200237, P. R. China. E-mail: wangjt@ecust.edu.cn; Fax: +86 21 64252914; Tel: +86 21 64252924

This journal is © The Royal Society of Chemistry 2017

Open Access Article. Published on 18 May 2017. Downloaded on 11/25/2024 9:47:15 PM.
This article is licensed under a Creative Commons Attribution-NonCommercial 3.0 Unported Licence.

cause long time chemical corrosion and energy consuming, meanwhile the destruction of expensive templates leads to high cost and low yield of scale-up. Therefore, such methods still remain the great challenge to exploit facile sustainable techniques to prepare hierarchical porous carbons.

Generally, to improve the specific surface area, the subsequent activation process is required. The common methods of activation include physical activation and chemical activation.[30–37] The physical activation process involves carbonization of the raw materials and the subsequent activation at high temperature in a carbon dioxide or steam atmosphere.[35–37] In the chemical activation process, a series of cross-linking and pyrolysis processes could happen quickly at lower temperature to create abundant pores.[30–34] Recently, low melting point salts, such as $ZnCl_2$, LiCl, KCl and NaCl, as activator, have been explored for the synthesis of porous materials with unique nanostructures.[38–42] Nevertheless, the typical activation reaction mainly carried out on the surface of materials, making it difficult to create appropriate and accessible pores in the bulk for ion diffusion and adsorption. Therefore, it is still eagerly welcomed to develop simple and low cost techniques to prepare hierarchical porous carbons with high surface area and satisfied porosity.

Herein, we developed a facile metal chloride-assisted method for efficient synthesis of hierarchical porous carbons through a simple sol–gel polymerization process followed *in situ* chemical activation during carbonization. The metal chlorides ($ZnCl_2$, $NiCl_2$, $FeCl_3$) were directly mixed with resorcinol and terephthaldehyde to form a homogeneous solution, and could act as reaction assistant to form 3D porous network particles. The hierarchical porous carbons could be obtained by direct carbonization and following acid washing, which inherit the 3D structure due to the rigidity of network. In the obtained carbons, the micropores are generated within the highly cross-linked network of polymer chains, while the mesopores and macropores are formed by the interconnected particles. The porous structure of the hierarchical porous carbons could be adjusted by adding different metal chlorides. Owing to the *in situ* chemical activation effect of $ZnCl_2$, the as-prepared hierarchical porous carbon possesses relatively high specific surface area and excellent electrochemical performance as electrode material. The metal chloride-assisted method provides a new idea for the preparation of hierarchical porous carbons *via* the time-saving, recyclable, *in situ* chemical activation process, which could have great potential for the supercapacitor and other energy storage applications.

2 Experimental section

2.1 Preparation of the hierarchical porous carbon materials

All chemicals were purchased from Titanchem Co. and used without further treatment. The polymer precursors were synthesized *via* a solvent-thermal method, using resorcinol (R) and terephthalaldehyde (T) as the carbon sources, metal chloride as reaction assistant and ethyl alcohol as solvent. In a typical synthesis, 20 mmol R, 40 mmol T and 10 g metal chloride were added to 80 mL ethyl alcohol under stirring at 40 °C for 20 min. Subsequently, the mixed solution was transferred into a 100 mL sealed Teflon-lined autoclave and heated at 180 °C for 24 h. The polymeric gel was obtained after autoclave cooling down to ambient temperature naturally. Then, the gel was dried in an oven at 60 °C for 24 h, followed by thermal treatment at 800 °C with a heating rate of 1 °C min^{-1} for 2 h under nitrogen flow. Finally, the product was washed with hydrochloric acid and deionized water to remove all the metal chloride and dried at 80 °C for 24 h. The hierarchical porous carbon materials obtained were denoted as RT-X, where X represents the addition of metal chloride, and the blank sample that synthesized just from terephthalaldehyde and resorcinol was named as RT.

2.2 Characterization

The scanning electron microscopy (SEM, JEOL JSM-7500F) and transmission electron microscopy (TEM, JEOL 2100F) were used to observe the morphology and microstructure of the samples, after grounding and drying.

Nitrogen adsorption–desorption isotherms were measured on a Quadrasorb SI analyser at 77 K. Before measurements, the samples were degassed under vacuum at 473 K for 12 h. The specific surface area was calculated by utilizing the Brunauer–Emmett–Teller (BET) method and total pore volume was estimated from adsorbed amount at $P/P_0 = 0.985$. The micropore specific surface area and volume were calculated by t-plot method. The mesopore volume and mesoporous pore size distribution were acquired from the desorption branch based on the Barrett–Joyner–Halenda (BJH) model, while the micropore pore size distribution were calculated by nonlocal density functional theory (NLDFT-cylindrical model).

The carbon (C) and oxygen (O) contents on the surface were measured by an Axis Ultra DLD X-ray photoelectron spectroscopy. The working voltage and current of X-ray source were 15 kV and 10 mA, respectively, and the operating pressure was lower than 2×10^{-8} Torr. The C 1s and O 1s XPS spectra were obtained at 0.1 eV step size. The multiple peak separation of O 1s were carried out by mixed Gaussian/Lorentzian curve fitting method, and the background was subtracted by Shirley function using a XPS peak processing software. The peak width was not fixed during the fit procedure.

The crystallographic structures were measured by the X-ray diffraction (XRD) patterns and Raman spectra. The XRD patterns were recorded by a Rigaku D/max 2550 diffractometer which working voltage and current were 40 kV and 20 mA and radiation is Cu Kα ($\lambda = 1.5406$ Å). Raman spectra were acquired on a Renishaw system 1000 with an argon-ion laser operating at 514 nm using a charged-coupling-device detector.

2.3 Electrochemical test

The electrode plates were composed of active material, acetylene black and polytetrafluoroethylene binder. Firstly, these materials were mixed in a mass ratio of 85 : 10 : 5 by adding a small amount of ethanol, and gradually ground in an agate mortar to form a homogeneous paste. Afterwards, the paste was turned into a film with a thickness of ~0.09 mm by the aid of

Open Access Article. Published on 18 May 2017. Downloaded on 11/25/2024 9:47:15 PM.
This article is licensed under a Creative Commons Attribution-NonCommercial 3.0 Unported Licence.

a roller press. The electrode plates were finally obtained through punching the film into small round with a diameter of ~8 mm and each of the electrode plate contained approximately 3 mg activated material. The simulative device for experiment constructed with two same electrode plates separated with a membrane. 3 mol L^{-1} H_2SO_4 was used as electrolyte in all the electrochemical experiment.

The cyclic voltammetry (CV) with voltage range from 0 V to 0.9 V and electrochemical impedance spectroscopy (EIS) analysis with frequency range of 0.01 Hz to 100 kHz were performed on a Gamry Instrument (Warminster, PA, USA). Galvanostatic charge–discharge at different current densities was carried out on an ARBIN BT2000 apparatus. The specific discharge capacitance of the sample was calculated from the following equation

$$C = It/m\mathrm{d}V \quad (1)$$

where C, I, t, m and dV represent the specific discharge capacitance (F g^{-1}), the discharge current (A), the discharge time (s), the mass of electrode (g) and the potential difference of single electrode (V), respectively.

3 Results and discussion

3.1 Characterization of the hierarchical porous carbon materials

Scheme 1 demonstrates the possible synthesis process of the hierarchical porous carbon by the aid of metal ion. The resorcinol and terephthaldehyde could crosslink each other into small cluster around the metal ion which has the unoccupied molecular orbital to attract the oxygen atom of resorcinol and terephthaldehyde. The cluster grows further *via* polymerizing into colloid-like polymer particles, followed by microphase separation to form 3-D gels[43,44]. The hierarchical porous carbons could be obtained by following carbonization and acid washing. In this work, both the reactants possess the benzene skeleton to improve the rigidity of the polymer backbone, which leads to the formation of stable network. The metal chloride acts as the reaction assistant of polymerization to form 3-D porous network. Moreover, it could also be recycled effectively through collecting the liquid waste. The synthesis process is simple and low-cost, which is promising to be employed for industrial-scale production.

The typical SEM and TEM images of the obtained RT and the RT-X carbons with different metal chlorides are shown in Fig. 1 and 2, respectively. From the SEM images, it could be observed that RT is normal carbon microsphere with smooth surface, while the RT-X carbons show typically 3-D porous networks formed by the inter-linking of irregular particles, and meso-macropores could also be clearly observed. The apparent difference between RT and RT-X of morphologies should be certainly ascribed to the addition of metal chloride, which could change the sol–gel reaction pathway to form the particles accumulation. The TEM images obviously show that the particle size gradually decreases with the increasing electronegativity of the different metal ions. It is because that the metal ion with higher electronegativity can help resorcinol and terephthalaldehyde polymerize with smaller space steric hindrance. Such result suggests that both the porous structure and particle size could be adjusted by different kind and amount of additives.

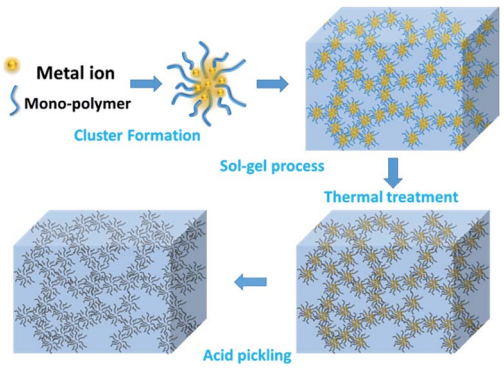

Scheme 1 The schematic illustration of the hierarchical porous carbon preparation.

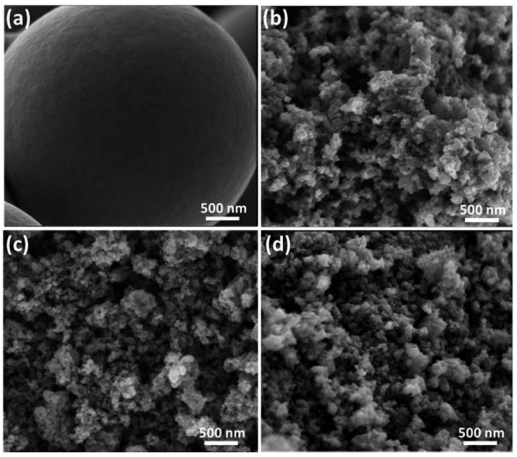

Fig. 1 SEM images of the samples (a) RT, (b) RT-$ZnCl_2$, (c) RT-$NiCl_2$, (d) RT-$FeCl_3$.

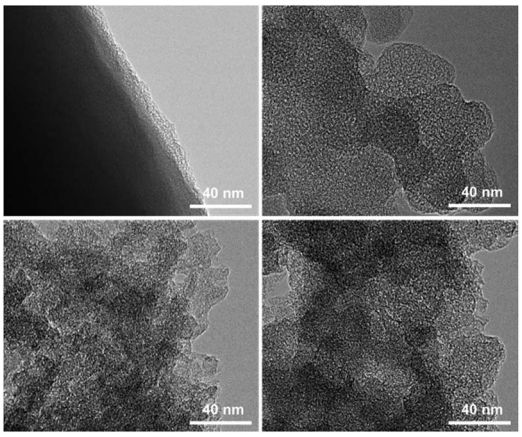

Fig. 2 TEM images of the samples (a) RT, (b) RT-$ZnCl_2$, (c) RT-$NiCl_2$, (d) RT-$FeCl_3$.

This journal is © The Royal Society of Chemistry 2017

Open Access Article. Published on 18 May 2017. Downloaded on 11/25/2024 9:47:15 PM.
This article is licensed under a Creative Commons Attribution-NonCommercial 3.0 Unported Licence.

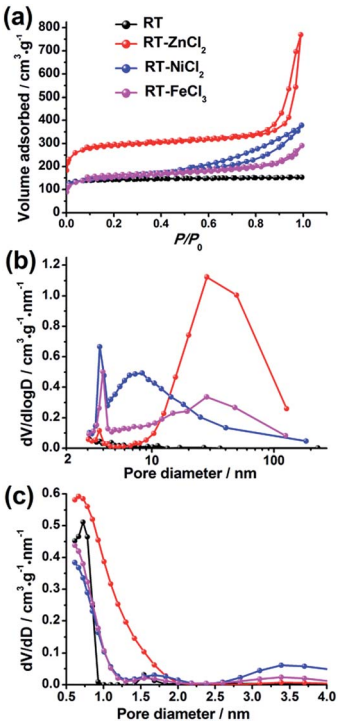

Fig. 3 (a) The N_2 adsorption–desorption isotherms, (b) the BJH and (c) NL-DFT pore size distributions.

The N_2 adsorption–desorption isotherms of the hierarchical porous carbons are presented in Fig. 3(a). The isotherm of RT is assigned to the typical type I responding to the single existence of abundant micropores. While the isotherms of RT-$ZnCl_2$, RT-$NiCl_2$ and RT-$FeCl_3$ belong to the type IV with associated H1 hysteresis loops which indicate the presence of mesopores formed from the particles stacking. In addition, the high uptake of N_2 adsorption at low relative pressures (0–0.1) and the slight increase at high relative pressure (0.9–1.0) indicate that micropores and macropores co-exist in the metal chloride-assisted samples. The pore size distributions calculated using BJH and DFT model are also shown in Fig. 3(b) and (c), respectively. It demonstrates that the addition of metal chloride leads to the formation of some mesopores. The calculated porosity parameters are listed in Table 1. The BET surface areas of RT, RT-$NiCl_2$ and RT-$FeCl_3$ are all *ca.* 550 $m^2\ g^{-1}$, and it increases to 1106 $m^2\ g^{-1}$ for RT-$ZnCl_2$. In addition, the average pore diameter calculated by BJH model and total volume of RT-$ZnCl_2$ are also the largest. This is because that the *in situ* $ZnCl_2$ activation could homogeneously and continuously take place in the polymer framework to generate amounts of appropriate pores during the carbonization process. The result reveals that the addition of metal chloride could introduce large amount of mesopores and macropores into porous carbon, formed by the inter-linking of irregular particles. Meanwhile, the specific area increases significantly in the presence of $ZnCl_2$ because of its unique *in situ* activation role which is different from the typical activation.

The element composition and chemical state on the surface were measured by high-resolution X-ray photoelectron spectroscopy (XPS), as shown in Fig. 4. The XPS survey scan spectra with binding energy ranging from 0 to 1000 eV show that there are only C and O on the surface of all samples. All the high-resolution XPS spectra of C 1s show very similar unimodal peak shapes at 284.8 eV, which is related to the graphitic carbon, suggesting that most carbon atoms exist in conjugated honeycomb lattices.[45] The O 1s peak could be curve-fitted into three peaks centered around 533.5, 532.3 and 530.8 eV which represent C–O–C, C–OH and C=O, respectively.[46] The content of C=O in RT-X increases with the increasing electronegativity of metal ion, while no C=O is resolved in RT, suggesting that the metal chloride could catalyze the C–OH dehydrogenation to form C=O and the catalytic performance is related to the electronegativity.

The crystallographic structures of all samples were demonstrated by XRD, as displayed in Fig. 5(a). All samples show two similar broadened diffraction peaks located at *ca.* 25.1° and 43.9°, corresponding to the reflections of the graphitic planes (002) and (100), respectively.[47] The addition of metal chloride doesn't change the position of two peaks. However, RT-$NiCl_2$ shows a little sharper peak suggesting that $NiCl_2$ could promote graphitization somewhat at high temperature. As shown in Fig. 5(b), Raman spectroscopy was carried out to further characterize the microcrystalline structures of all samples. The peak at 1350 cm^{-1} (D-band) is associated with the amorphous carbon, while the peak at 1581 cm^{-1} (G-band) is attributed to ordered graphite in-plane vibrations with E_{2g} symmetry.[48] Therefore, the disordered degree of carbon materials could be characterized with the intensity ratios of the D-band to the G-band (I_D/I_G). The I_D/I_G ratios of RT, RT-$ZnCl_2$, RT-$NiCl_2$ and RT-$FeCl_3$ calculated from the peak area are 2.95, 3.61, 2.40 and 2.62, respectively. The result suggests that all samples are amorphous carbon and the addition of $ZnCl_2$ could introduce more defectiveness to the porous carbon because of its *in situ* activation, while the $NiCl_2$ and $FeCl_3$ could increase the degree of graphitization due to their catalytic graphitization.

Table 1 Pore parameters of the hierarchical porous carbons

Sample	S_{BET}[a] ($m^2\ g^{-1}$)	V_T[b] ($cm^3\ g^{-1}$)	S_{mic}[c] ($m^2\ g^{-1}$)	V_{mic}[d] ($cm^3\ g^{-1}$)	D_{DFT}[e] (nm)	V_{meso}[f] ($cm^3\ g^{-1}$)	D_{BJH}[g] (nm)
RT	558	0.24	523	0.21	0.67	0.02	3.2
RT-$ZnCl_2$	1106	1.19	960	0.39	0.67	0.78	28.3
RT-$NiCl_2$	591	0.59	375	0.15	0.67	0.42	3.8
RT-$FeCl_3$	572	0.45	434	0.18	0.67	0.22	7.4

[a] BET specific surface area from N_2 adsorption. [b] Total pore volume ($P/P_0 = 0.985$). [c] DFT micropore surface area (<2 nm). [d] DFT micropore volume (<2 nm). [e] DFT pore diameter. [f] BJH mesopore volume. [g] BJH pore diameter.

Open Access Article. Published on 18 May 2017. Downloaded on 11/25/2024 9:47:15 PM.
This article is licensed under a Creative Commons Attribution-NonCommercial 3.0 Unported Licence.

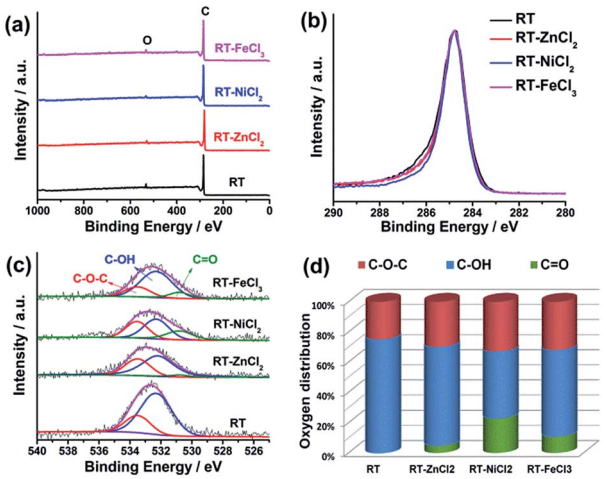

Fig. 4 (a) XPS survey, (b) high-resolution C 1s, (c) high-resolution O 1s spectra, (d) the distribution of O species in the samples from resolving peaks of the O 1s spectra.

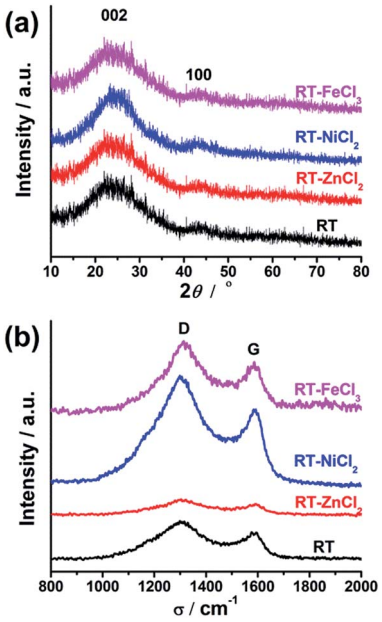

Fig. 5 XRD (a) and Raman (b) spectra of the samples.

3.2 The electrochemical performances

In the hierarchical porous structure, macropores provide a high volume to store electrolyte so as to shorten the diffusion distance of ion, while mesopores are necessary for fast ion transport, and micropores contribute high surface area to adsorb amounts of ions. Such unique properties indicate that the hierarchical porous carbons could be ideal electrode materials for high-performance supercapacitors. In order to examine the electrochemical properties of the as-prepared hierarchical porous carbons as supercapacitor electrode materials, various electrochemical measurements, such as galvanostatic charge–discharge (GCD), cyclic voltammetry (CV) and electrochemical impedance spectroscopy (EIS), were carried out in a two-electrode configuration using 3 mol L^{-1} H_2SO_4 as electrolyte.

All the cyclic voltammetry curves tested in the voltage range of 0–0.9 V at the scan rates of 10 mV s^{-1} and 100 mV s^{-1} are illustrated in Fig. 6. It can be observed that all the CV curves present quasi-rectangular shapes at scan rate of 10 mV s^{-1}, indicating the formation of electric double layer. Furthermore, the area of CV curve which reflects the specific capacitance increases with the increasing of micropore specific area. However, when the scan rate increases from 10 mV s^{-1} to 100 mV s^{-1}, the CV curve of RT presents obvious deformation and minimum area due to high resistance for the ion diffusing into the narrow micropores. While the CV curves of RT-X carbons still maintain roughly rectangular shapes, suggesting that the electrolyte ions could more easily diffuse into the micropores of metal chloride-assisted samples to form electric double layer. The result indicates that the micro-meso-macroporous network formed by the inter-linking of irregular particles is quite adequate architecture for ion diffusion resulting in excellent rate capability.

The electrochemical behaviors of the samples were further investigated by galvanostatic charge–discharge measurements, which could be used to calculate the specific capacitance, power density and energy density. The charge–discharge curves at the current density of 1 A g^{-1} and 10 A g^{-1} are shown in Fig. 7(a) and (b), respectively. All the samples demonstrate symmetric charge–discharge curves at 1 A g^{-1}, indicating the standard electric double layer behavior. But when the current density increases to 10 A g^{-1}, the obvious warp and IR drop can be detected in the charge–discharge curve of RT due to the high diffusion resistance in narrow micropores, quite agreeing with the result of CV measurement. While those of the metal chloride-assisted samples still remain symmetrical isosceles triangle with negligible IR drop, clarifying that the hierarchical porous carbons have good capacitive behavior with little energy loss even at high current density. The rate capability of different

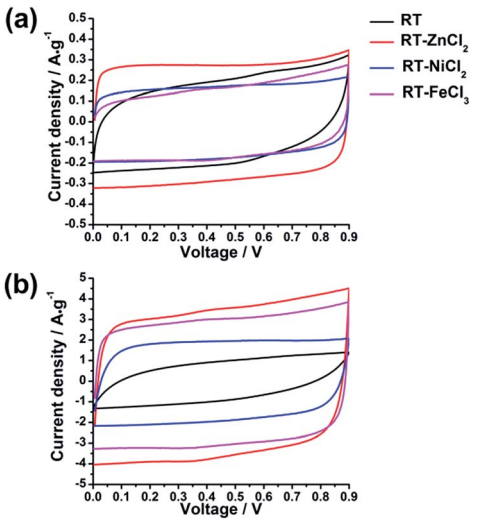

Fig. 6 The cyclic voltammetry curves of different samples at (a) 10 mV s^{-1} and (b) 100 mV s^{-1}.

This journal is © The Royal Society of Chemistry 2017

Open Access Article. Published on 18 May 2017. Downloaded on 11/25/2024 9:47:15 PM.
This article is licensed under a Creative Commons Attribution-NonCommercial 3.0 Unported Licence.

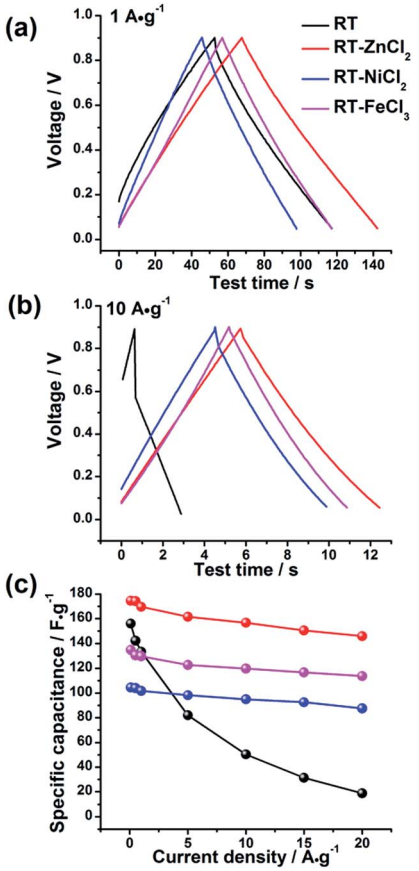

Fig. 7 The galvanostatic charge–discharge curves of all samples at (a) 1 A g^{-1} and (b) 10 A g^{-1} and (c) the rate capability.

samples calculated from galvanostatic discharge measurements is compared in Fig. 7(c). The specific capacitances of RT, RT-$ZnCl_2$, RT-$NiCl_2$ and RT-$FeCl_3$ at the current density of 0.1 A g^{-1} are 156.1 F g^{-1}, 174.6 F g^{-1}, 104.5 F g^{-1} and 134.8 F g^{-1}, respectively. The obtained capacitances of all samples are positively correlated with the micropore specific area because the ions are mainly adsorbed by micropores. When the current density reaches 20 A g^{-1}, the capacitance of RT reduces to 18.7 F g^{-1}, only 12% of the capacitance can be maintained. In addition, the

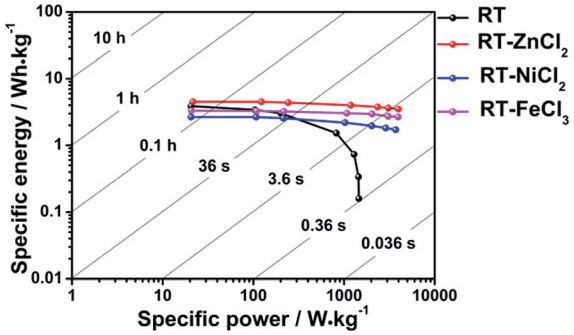

Fig. 8 The Ragone plots of the cells using different samples as electrode materials.

capacitances of all the metal chloride-assisted samples could retain as high as *ca.* 84%, due to the fast ion diffusion. This rate capability is better than that of many hierarchical porous carbons reported in previous literatures, as listed in Table 2. Such excellent rate capability is much to be desired for the practical application of supercapacitor. These results suggest that the narrow micropores in RT are remarkably disadvantageous for ion diffusion and the addition of metal chloride could create approachable channels for ion rapidly diffusing into the micropores to achieve superior rate capability. In addition, highest capacitance of 174.6 F g^{-1} is acquired by adding zinc chloride with additional *in situ* activation role.

The Ragone plots which visually reflect the energy and power output capability of supercapacitor are shown in Fig. 8. The energy density and power density are calculated from discharge measurements based on the followed equation.

$$E = \frac{1}{2 \times 3.6} \times CV^2 \quad (2)$$

$$P = E/t \quad (3)$$

where E, C, V, P and t respectively represent gravimetric energy density (W h kg^{-1}), gravimetric specific capacitance of cell (F g^{-1}), the voltage change in discharge (V), gravimetric power density (W kg^{-1}) and the discharge time (h).

Table 2 The rate capabilities of various hierarchical porous carbons

Precursor	Fabrication	Retention	Current density	Electrolyte	Ref.
Terephthalaldehyde, resorcinol	Dual roles of $ZnCl_2$: Reaction assistant and *in situ* chemical activation	*ca.* 84%	0.1–20 A g^{-1}	3 M H_2SO_4	This work
Resol	Silica and P123 as multi-templates	*ca.* 24%	0.2–6 A g^{-1}	5 M KOH	18
Furfuryl alcohol	Silica, PAA and CTAB as multi-templates, KOH as activation agent	*ca.* 68%	0.5–10 A g^{-1}	6 M KOH	19
Phenol, formaldehyde	Silica as template	*ca.* 71%	1–10 A g^{-1}	6 M KOH	27
Phenolic resin	F127 as template and KOH as activation agent	*ca.* 72%	0.2–20 A g^{-1}	6 M KOH	32
Terephthalaldehyde, melamine, pyrrolidine	$ZnCl_2$ as activation agent	*ca.* 76%	1–10 A g^{-1}	1 M H_2SO_4	33
Enteromorpha	$ZnCl_2$ as activation agent	*ca.* 79%	0.4–1 A g^{-1}	6 M KOH	38
Resorcinol, formaldehyde	$ZnCl_2$ as activation agent	*ca.* 62%	0.5–20 A g^{-1}	2 M KOH	39
Chitosan	$ZnCl_2$ as activation agent	*ca.* 75%	0.5–20 A g^{-1}	6 M KOH	41

Open Access Article. Published on 18 May 2017. Downloaded on 11/25/2024 9:47:15 PM.
This article is licensed under a Creative Commons Attribution-NonCommercial 3.0 Unported Licence.

All cells show maximum energy density at minimum current density because ions could be adsorbed by micropores as many as possible. The largest power density is achieved at maximum current density due to the fastest speed of charges transfer. It is obvious that the addition of metal chloride could improve the ability of power output and energy storage capacity at high current density. Among them, the cell used RT-$ZnCl_2$ as electrode material possesses maximum energy density (4.5 W h kg^{-1} at 0.1 A g^{-1}) and power density (3987.6 W kg^{-1} at 20 A g^{-1}).

To detailedly reveal the charge–discharge kinetics inside the electrode, the electrochemical impedance spectroscopy (EIS) was measured with the frequency ranging from 0.01 Hz to 100 kHz. As displayed in Fig. 9a and b, the electrochemical impedance of supercapacitor could be divided into three parts in the Nyquist plots: electrolyte resistance (*x*-intercept at the highest frequency region), interfacial contact impedance of electrode material (semicircle at the middle frequency region), and the diffusion resistance which is associated with intra-particle pores (oblique line at the low frequency region).[49,50] The values of interfacial contact impedance for RT, RT-$ZnCl_2$, RT-$NiCl_2$ and RT-$FeCl_3$ are 0.27 Ω cm^{-2}, 0.19 Ω cm^{-2}, 0.17 Ω cm^{-2} and 0.18 Ω cm^{-2}, respectively, suggesting the semicircles may be also partly associated with ionic dynamic dispersion within the pores.[51] Different from the flexuous curve of RT, the vertical lines of all the metal chloride-assisted samples appear at the low frequency region. It is attributed to the satisfying channels in the metal chloride-assisted hierarchical porous carbons for ion diffusion, while the narrow micropores in RT are difficult for ion diffusing to form electric double layer.

The Bode plots, which describe the evolution of the real capacitances (C') and the imaginary capacitances (C'') with frequency changing, are adopted to further studying the ion diffusion kinetics in different samples, as shown in Fig. 9c and d. The capacitance of cell (C) is defined by Kronig–Kramers relational expression ($C = C' - jC''$).[51,52] The evolution of C'/C_{max}' with frequency corresponds to the process of cell changing from pure resistive behavior ($C'/C_{max}' = 0$) to pure capacitive behavior ($C'/C_{max}' = 1$). At the region of high frequency (>100 Hz), the time is too short for the ions to diffuse into the micropores of electrodes, so that the cell works as a pure resistance. In contrast, the ions could be adsorbed as many as possible at low frequency, therefore the cell could be regarded as a pure capacitor. Generally, when the value of real capacitance exceeds 50% of C_{max}', the device performs more like a capacitor rather than a resistance. Thus, the corresponding frequency ($f_{0.5}$) could be used to evaluate the capability of rapid charging and discharging. The $f_{0.5}$ for RT, RT-$ZnCl_2$, RT-$NiCl_2$ and RT-$FeCl_3$ are 0.03 Hz, 1.04 Hz, 1.81 Hz and 0.49 Hz, respectively. According to the Kronig–Kramers relational expression, the imaginary capacitance could denote the energy dissipation in the process of pure resistive behavior changing to pure capacitive behavior. The maximum energy loss appeared at the frequency of $f_{0.5}$ which reciprocal defines the relaxation time constant (τ_0). The τ_0 values for RT, RT-$ZnCl_2$, RT-$NiCl_2$ and RT-$FeCl_3$ are 32.05 s, 0.96 s, 0.55 s and 2.04 s, respectively. These results give valuable insight into the role of developed meso-macropores on the acceleration of ion transport with the addition of metal chloride in synthesis.

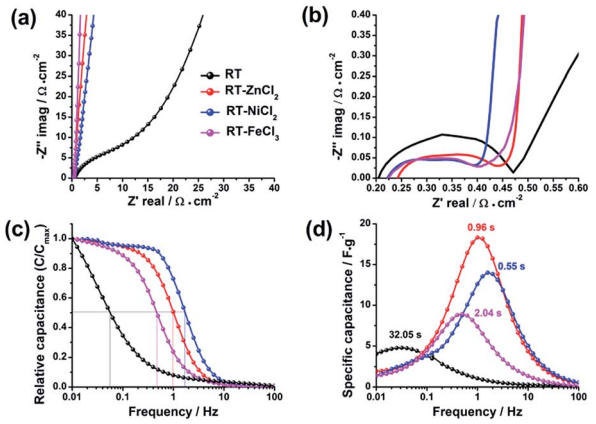

Fig. 9 (a) Nyquist plots, (b) the enlargement of the high-frequency region, (c) evolution of the relative real capacitance and (d) imaginary capacitance with frequency of all samples.

4 Conclusions

With the addition of metal chloride, hierarchical porous carbons were successfully prepared through a typical sol–gel process and subsequent *in situ* activation during carbonization, using terephthalaldehyde and resorcinol as the carbon precursors. The presence of metal chloride could efficiently help to form the developed micro-meso-macroporous structure by particles stacking. Such hierarchical porosity plays an important role for rapid ion diffusion, resulting in excellent rate capability and low diffusion resistance. All the metal chloride-assisted hierarchical porous carbons maintain excellent rate capability of *ca.* 84% retention from 0.1 A g^{-1} to 20 A g^{-1}, higher than that of many hierarchical porous carbons reported in previous literatures. $ZnCl_2$ could also act as the *in situ* activation agent during the thermal treatment process to develop high surface area of 1106 m^2 g^{-1}, and large pore volume of 1.2 cm^3 g^{-1}. Therefore, the RT-$ZnCl_2$ could serve as the ideal electrode material with the highest specific capacitance of 174.6 F g^{-1}, maximum energy output capability (4.5 W h kg^{-1} at 0.1 A g^{-1}) and outstanding power output capability (3987.6 W kg^{-1} at 20 A g^{-1}) in 3 mol L^{-1} H_2SO_4. These results illustrate that the metal chloride-assisted hierarchical porous carbons with developed 3-D networks have great potential in the application of electrochemical energy storage.

Acknowledgements

This work was financially supported by MOST (2014CB239702), National Natural Science Foundation of China (No. 21506061, 21576090, 51302083, 51272077), Shanghai Municipal Natural Science Foundation (No. 14ZR1410400), Shanghai Rising-Star Program (17QB1401700), Petro China Innovation Foundation and Fundamental Research Funds for the Central Universities.

 This journal is © The Royal Society of Chemistry 2017

Open Access Article. Published on 18 May 2017. Downloaded on 11/25/2024 9:47:15 PM.
This article is licensed under a Creative Commons Attribution-NonCommercial 3.0 Unported Licence.

References

1 G. P. Hao, Z. Y. Jin, Q. Sun, *et al.*, *Energy Environ. Sci.*, 2013, **6**, 3740–3747.
2 M. E. Casco, M. Martínez-Escandell, J. Silvestre-Albero, *et al.*, *Carbon*, 2014, **67**, 230–235.
3 C. Zhu, H. Li, S. Fu, *et al.*, *Chem. Soc. Rev.*, 2016, **45**, 517–531.
4 E. Lam and J. H. T. Luong, *ACS Catal.*, 2014, **4**, 3393–3410.
5 S. K. Gordeev, *Met. Sci. Heat Treat.*, 2015, **56**, 559–563.
6 S. W. Ryter and L. E. Otterbein, *BioEssays*, 2004, **26**, 270–280.
7 S. Han, D. Wu, S. Li, *et al.*, *Adv. Mater.*, 2014, **26**, 849–864.
8 M. Zeiger, N. Jäckel, V. N. Mochalin, *et al.*, *J. Mater. Chem. A*, 2016, **4**, 3172–3196.
9 L. L. Zhang and X. S. Zhao, *Chem. Soc. Rev.*, 2009, **38**, 2520–2531.
10 C. Liang, Z. Li and S. Dai, *Angew. Chem., Int. Ed.*, 2008, **47**, 3696–3717.
11 M. Zhi, C. Xiang, J. Li, *et al.*, *Nanoscale*, 2013, **5**, 72–88.
12 M. M. Sk, C. Y. Yue, K. Ghosh, *et al.*, *J. Power Sources*, 2016, **308**, 121–140.
13 P. Simon and Y. Gogotsi, *Nat. Mater.*, 2008, **7**, 845–854.
14 E. Frackowiak, *Phys. Chem. Chem. Phys.*, 2007, **9**, 1774–1785.
15 G. Wang, L. Zhang and J. Zhang, *Chem. Soc. Rev.*, 2012, **41**, 797–828.
16 A. González, E. Goikolea, J. A. Barrena, *et al.*, *Renewable Sustainable Energy Rev.*, 2016, **58**, 1189–1206.
17 Q. Wang, J. Yan, Y. Wang, *et al.*, *Carbon*, 2014, **67**, 119–127.
18 W. Zhou, Z. Lin, G. Tong, *et al.*, *RSC Adv.*, 2016, **6**, 111406–111414.
19 J. Liu, X. Wang, J. Gao, *et al.*, *Electrochim. Acta*, 2016, **211**, 183–192.
20 Q. Zhao, X. Wang, J. Liu, *et al.*, *Electrochim. Acta*, 2015, **154**, 110–118.
21 W. Tian, Q. Gao, Y. Tan, *et al.*, *J. Mater. Chem. A*, 2015, **3**, 5656–5664.
22 Y. Wang, S. Tao, Y. An, *et al.*, *J. Mater. Chem. A*, 2013, **1**, 8876–8887.
23 H. J. Liu, J. Wang, C. X. Wang, *et al.*, *Adv. Energy Mater.*, 2011, **1**, 1101–1108.
24 D. D. Zhou, H. J. Liu, Y. G. Wang, *et al.*, *J. Mater. Chem.*, 2012, **22**, 1937–1943.
25 R. Ruiz-Rosas, M. J. Valero-Romero, D. Salinas-Torres, *et al.*, *ChemSusChem*, 2014, **7**, 1458–1467.
26 D. Xu, S. Che and O. Terasaki, *New J. Chem.*, 2016, **40**, 3982–3992.
27 Y. Han, S. Liu, D. Li, *et al.*, *Electrochim. Acta*, 2014, **138**, 193–199.
28 M. J. Valero-Romero, E. M. Márquez-Franco, J. Bedia, *et al.*, *Microporous Mesoporous Mater.*, 2014, **196**, 68–78.
29 S. Wang, T. Wang, P. Liu, *et al.*, *Mater. Res. Bull.*, 2017, **88**, 62–68.
30 P. Hao, Z. Zhao, J. Tian, *et al.*, *Nanoscale*, 2014, **6**, 12120–12129.
31 L. Qie, W. Chen, H. Xu, *et al.*, *Energy Environ. Sci.*, 2013, **6**, 2497–2504.
32 X. Yu, J. Lu, C. Zhan, *et al.*, *Electrochim. Acta*, 2015, **182**, 908–916.
33 J. S. Wei, H. Ding, Y. G. Wang, *et al.*, *ACS Appl. Mater. Interfaces*, 2015, **7**, 5811–5819.
34 M. Sevilla and R. Mokaya, *Energy Environ. Sci.*, 2014, **7**, 1250–1280.
35 T. Tooming, T. Thomberg, H. Kurig, *et al.*, *J. Power Sources*, 2015, **280**, 667–677.
36 K. Xia, Q. Gao, J. Jiang, *et al.*, *Carbon*, 2008, **46**, 1718–1726.
37 Z. Y. Sui, Q. H. Meng, J. T. Li, *et al.*, *J. Mater. Chem. A*, 2014, **2**, 9891–9898.
38 M. Wu, P. Li, Y. Li, *et al.*, *RSC Adv.*, 2015, **5**, 16575–16581.
39 Y. Wang, B. Chang, D. Guan, *et al.*, *J. Solid State Electrochem.*, 2015, **19**, 1783–1791.
40 X. Liu and M. Antonietti, *Carbon*, 2014, **69**, 460–466.
41 X. Deng, B. Zhao, L. Zhu, *et al.*, *Carbon*, 2015, **93**, 48–58.
42 T. Ouyang, K. Cheng, Y. Gao, *et al.*, *J. Mater. Chem. A*, 2016, **4**, 9832–9843.
43 J. Wang, S. Xu, Y. Wang, *et al.*, *RSC Adv.*, 2014, **4**, 16224–16232.
44 X. Bing, Y. Wei, M. Wang, *et al.*, *J. Colloid Interface Sci.*, 2017, **488**, 207–217.
45 M. Wang, J. Wang, W. Qiao, *et al.*, *RSC Adv.*, 2014, **4**, 61456–61464.
46 D. Hulicova-Jurcakova, M. Seredych, G. Q. Lu, *et al.*, *Adv. Funct. Mater.*, 2009, **19**, 438–447.
47 H. Chen, F. Sun, J. Wang, *et al.*, *J. Phys. Chem. C*, 2013, **117**, 8318–8328.
48 K. Mcguire, N. Gothard, P. Gai, *et al.*, *Carbon*, 2005, **43**, 219–227.
49 H. K. Song, H. Y. Hwang, K. H. Lee, *et al.*, *Electrochim. Acta*, 2000, **45**, 2241–2257.
50 Z. Hu, X. Xiao, C. Chen, *et al.*, *Nano Energy*, 2015, **11**, 226–234.
51 H. Wu, X. Wang, L. Jiang, *et al.*, *J. Power Sources*, 2013, **226**, 202–209.
52 P. L. Taberna, P. Simon and J. F. Fauvarque, *J. Electrochem. Soc.*, 2003, **150**, A292–A300.